Journal of Materials Chemistry A

PAPER

View Article Online
View Journal | View Issue

Cite this: J. Mater. Chem. A, 2018, 6, 4776

A yolk–shelled Co_9S_8/MoS_2–CN nanocomposite derived from a metal–organic framework as a high performance anode for sodium ion batteries†

Yuyu Wang, Wenpei Kang,* Dongwei Cao, Minghui Zhang, Zixi Kang, Zhenyu Xiao, Rongming Wang* and Daofeng Sun

Received 16th January 2018
Accepted 17th February 2018

DOI: 10.1039/c8ta00493e

rsc.li/materials-a

Sodium-ion batteries (SIBs) are considered as a promising energy storage device, and anode materials are proved to essentially affect their electrochemical performance. In this work, a yolk–shell structured Co_9S_8/MoS_2 polyhedron with N-doped carbon composite (Co_9S_8/MoS_2–CN) was designed and synthesized through a step by step process using ZIF-67 as the precursor. And this composite is demonstrated to be an excellent electrode candidate material for SIBs due to the magnificent yolk–shelled structures, *in situ* CN coating and the synergistic effect of the binary sulfides. The Co_9S_8/MoS_2–CN composite electrode shows highly stable cycling performance and delivers a reversible discharge capacity of 438 mA h g^{-1} within 150 cycles at a current density of 1.0 A g^{-1}, which is much higher than that of Co_9S_8–CN or MoS_2 electrodes. Even at a high current density of 2.0 A g^{-1}, it can also deliver an impressively stable capacity of 421 mA h g^{-1} within 250 cycles.

Introduction

With the high demand for secondary batteries in the energy storage market, sodium ion batteries (SIBs) have been receiving more and more attention from researchers, because they possess a similar energy storage mechanism to lithium ion batteries (LIBs). In addition, the abundant and widespread sodium resources make the cost of SIBs lower, promoting their application in large scale energy storage fields in the future.[1–3] However, the inferior limits including the larger ionic radius and higher molar mass of sodium still hinder the development of SIBs and their practical application.[4–6] Generally, one of the most effective methods to improve the electrochemical performance of SIBs is to design suitable electrode materials, especially explore suitable anode materials with high specific capacity, long cycle life and excellent rate performance.[7,8]

Various alternative anode materials, such as carbon-based materials,[9–11] metal oxides (*e.g.*, CuO, TiO_2, and Co_3O_4)[12–14] and metal sulfides (*e.g.*, VS_4, CuS, FeS_2, and SnS),[15–18] have attracted our extensive attention due to their higher theoretical specific capacities and facile preparation processes. Among them, transition metal sulfides with the conversion reaction mechanism are of particular interest, as they possess higher capacities than traditional intercalation compounds through multiple electron transfer per metal centre and more suitable redox potentials as well as higher intrinsic conductivities than oxide anodes.[19,20] However, in order to obtain better performance, both construction of metal sulfide nanostructures and forming carbon-based composites were considered to be effective approaches.[21–24] Because the carbon materials can adsorb and capture the polysulfide intermediates, which are responsible for the shuttle effect, the nanostructures can endure the volume change during the sodiation/desodiation processes, consequently leading to a prolonged cycle life of the metal sulphide anodes.

Metal–organic frameworks (MOFs), as an emerging class of porous materials composed of metal ions and organic bridging ligands, have attracted our great interest due to their high surface areas, adjustable pore sizes and tunable structures.[25–27] Using MOFs as the precursors to prepare metal sulfides, porous, hollow and core–shell nanostructures can be easily obtained through a simple thermal decomposition process, and the heteroatom-doped carbon layers in the nanostructures can also be *in situ* transformed from the ligands.[28–32] Generally, MOF-derived materials can exhibit impressive performance based on the structural advantages when used as active materials for energy storage.[33–37] On the one hand, the derived nanostructures can shorten the diffusion path of Li^+/Na^+ ions and endure the volume expansion originated from the Li^+/Na^+ insertion. On the other hand, the heteroatom-doped carbon layer can increase the conductivity of metal sulphide anodes and present more active sites between Li^+/Na^+ ions and the electrolyte to improve the charge transfer efficiency during discharging and charging processes. For instance, Lai's group fabricated a 3-dimensional core–shell carbon-Co_xS_y/DPC using ZIF-67 as the precursor.[38]

College of Science, China University of Petroleum (East China), Qingdao 266580, P. R. China. E-mail: wpkang@upc.edu.cn; rmwang@upc.edu.cn

† Electronic supplementary information (ESI) available: Fig. S1–S8. See DOI: 10.1039/c8ta00493e

When used as the anode material for SIBs, it delivered a stable capacity of 300 mA h g^{-1} at 0.5 A g^{-1} after 50 cycles. Pan's group successfully synthesized ZnS nanoparticles decorated on N-doped porous carbon polyhedra using ZIF-8 as the reactant template. As an anode material for SIBs, it exhibited a desirable capacity of 370.6 mA h g^{-1} after 100 cycles at 0.1 A g^{-1} and 289.2 mA h g^{-1} after 1000 cycles at 1.0 A g^{-1}.[39] Moreover, a bimetallic sulfide composite ZnS–Sb_2S_3@C derived from ZIF-8 was reported by Yin's group.[40] Based on the unique structure and synergistic effect, ZnS–Sb_2S_3@C exhibited an excellent sodium storage capability with a high specific capacity of 630 mA h g^{-1} even after 120 cycles at 0.1 A g^{-1}.

In this work, a yolk–shelled Co_9S_8/MoS_2 polyhedron with N-doped carbon composite (Co_9S_8/MoS_2–CN) was prepared using ZIF-67 as the precursor through a step by step process, including carbonization of ZIF-67, hydrothermal reaction to form a MoS_2 layer, and sulfidation reaction at high temperature. As an anode material, Co_9S_8/MoS_2–CN shows a high and stable capacity of 438 mA h g^{-1} within 150 cycles at 1.0 A g^{-1}. Even at a high current density of 2.0 A g^{-1}, a capacity of 421 mA h g^{-1} can also be maintained after 250 cycles. The outstanding sodium storage performance can be attributed to the yolk–shelled structures of the Co_9S_8/MoS_2–CN composite, which is beneficial for: (i) lowering diffusion energy barriers and facilitating fast Na^+ insertion/extraction reaction kinetics, (ii) providing enough void space to accommodate volume changes upon sodiation/desodiation, (iii) improving electronic conductivity after *in situ* carbon modification, (iv) capturing the polysulfide intermediates, and (v) producing the synergistic effect.

Experimental

Synthesis of the ZIF-67 precursor and Co–CN composite

The ZIF-67 precursor was prepared using a simple precipitation method.[41] In a typical procedure, $Co(NO_3)_2 \cdot 6H_2O$ (1164 mg, 4.0 mmol) and 2-methylimidazole (1642 mg, 20.0 mmol) were respectively dissolved in methanol (100 mL) to form clear solutions, and then the two solutions were mixed and stirred at room temperature for 24 hours. Then the purple precipitate was collected by centrifugation, washed three times with ethanol and finally dried at 80 °C. The Co–CN precursor was obtained through a thermal decomposition of ZIF-67 at 500 °C with a heating rate of 1 °C min^{-1} under a N_2 atmosphere for 6 h.

Synthesis of yolk–shelled Co_9S_8/MoS_2–CN

30 mg of the above Co–CN precursor and 60 mg of $(NH_4)_2MoS_4$ were added to *N*,*N*-dimethylformamide (DMF, 30 mL) and sonicated for 15 min to form a uniform solution. Then the solution was transferred into a tightly sealed Teflon autoclave and maintained at 200 °C for 20 h. A black precipitate was collected by centrifugation, washed three times with deionized (DI) water and then dried in a vacuum freeze dryer. Finally, the product (30 mg) and sulfur powder (60 mg) were placed on two separate porcelain boats in a tube furnace and calcined at 600 °C with a heating rate of 1 °C min^{-1} in a H_2/Ar flow for 2 h. The Co_9S_8–CN polyhedron was prepared using ZIF-67 as the precursor. MoS_2 was also obtained through a solvothermal reaction except for the addition of the ZIF-67 precursor.

Materials characterization

The phase of the samples was examined by X-ray diffraction (XRD) on a Rigaku Ultima IV X-ray diffractometer. X-ray photoelectron spectroscopy (XPS) was carried out with a Thermo ESCALAB 250 surface analysis system. Inductively coupled plasma-mass spectrometry (ICP-MS) results were collected *via* an Optima 8000 spectrometer. The thermogravimetric analysis curve (TGA) was recorded by using a PerkinElmer TGA 7 in an air atmosphere (10 °C min^{-1}). To examine the morphology of the samples, SEM and TEM images were collected *via* a scanning electron microscope (Philips XL30 FEG SEM) and transmission electron microscope (JEOL JEM-2100 TEM), respectively. Raman spectra were collected *via* a HORIBA Evolution Raman spectroscope using the 532 nm incident wavelength. The N_2 adsorption–desorption isothermal curve at 77 K was collected by using a Micro ASAP2020 to calculate the BET surface area of the Co_9S_8/MoS_2–CN composite.

Electrochemical measurements

The working electrode was prepared as follows. The active material, carbon black, and sodium carboxymethyl cellulose (CMC) were mixed in DI water at a weight ratio of 6 : 2 : 2 to form a slurry, which was coated on Cu foil. The coated foil was dried at 80 °C and then cut into discs in a size of 12 mm. The coin cells were assembled in an Ar-glovebox. $NaClO_4$ (1.0 mol L^{-1}) dissolved in propylene carbonate with 10% (in volume) fluoroethylene carbonate (FEC) was used as the electrolyte. Galvanostatic discharge/charge cycling was performed using a Neware-5 V10 mA system (Shenzhen Xinwei). Cyclic voltammetry (CV) curves were measured on a Gamry 30115 electrochemical workstation (0.0–3.0 V) at a scan rate of 0.1 mV s^{-1}. Electrochemical impedance spectroscopy (EIS) was carried out on the Gamry 30115 electrochemical workstation with frequencies of 0.1 MHz to 10 mHz.

Results and discussion

The yolk–shelled Co_9S_8/MoS_2–CN nanostructure was prepared through a step by step process as shown in Fig. 1. ZIF-67 was firstly carbonized in order to obtain the *in situ* carbon transformed from the ligands, producing Co–CN as shown in Fig. S1.† The MoS_2 layer was formed after a subsequent solvothermal reaction. And the yolk–shelled Co_9S_8/MoS_2–CN nanostructure was obtained through sulfidation reaction with S powder at the upstream in the tube furnace.

The morphology of the Co_9S_8/MoS_2–CN composite was determined by scanning electron microscopy (SEM) and transmission electron microscopy (TEM) as shown in Fig. 2. Fig. 2a shows the SEM image of the Co_9S_8/MoS_2–CN sample, representing a general polyhedral morphology with a uniform size of ~400 nm, which is basically inherited from the structure of the ZIF-67 precursor (Fig. S2†). And the surfaces of the polyhedra

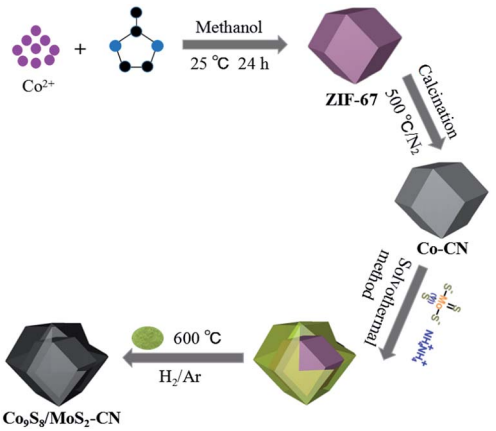

Fig. 1 Schematic diagram of the preparation of the yolk–shelled Co_9S_8/MoS_2–CN nanostructure.

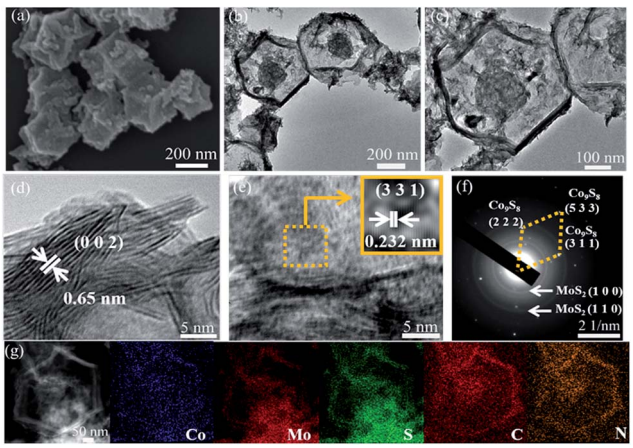

Fig. 2 (a) SEM image, (b, c) TEM images, (d, e) HRTEM images, (f) SAED patterns, and (g) EDS mapping images of the yolk–shelled polyhedral Co_9S_8/MoS_2–CN nanocomposite.

are rough, which is different from the ZIF-67, Co–CN and Co_9S_8–CN. As shown in Fig. S2a and b,† the as-prepared ZIF-67 possesses a homogeneous polyhedral structure with a smooth surface. Fig. S2d and e† also show well uniform sized Co–CN and Co_9S_8–CN polyhedra, greatly retaining the morphology of the ZIF-67 precursor. In addition, Co–CN and Co_9S_8–CN samples are both solid (Fig. S3†). The structure of the Co_9S_8/MoS_2–CN composite was further studied by TEM. A low magnification TEM image (Fig. 2b) shows typical yolk–shelled polyhedral structures, which is mainly based on the heterogeneous contraction caused by different components in the composite during the heat treatment process.[42] In the heat treatment process, the residual stress arose from the phase transformation and adhesion force will lead to product structure spallation, resulting in yolk–shelled structures. In a magnified TEM image (Fig. 2c), the nanosheets on the surface of the polyhedra can be observed, indicating the formation of MoS_2. High-resolution transmission electron microscopy (HRTEM) images of the yolk–shelled polyhedra are presented in Fig. 2d and e. For the surface part, the lattice fringe spacings are estimated to be 0.65 nm, corresponding to a (002) interlayer spacing of MoS_2 (Fig. 2d). For the inner part, after filtration treatment, lattice fringes with a spacing of 0.232 nm correspond well to the (331) planes of the Co_9S_8 phase. The corresponding selected-area electron diffraction (SAED) pattern is shown in Fig. 2f. Two phases of MoS_2 and Co_9S_8 can be indexed. The diffraction rings correspond to the (100) and (110) planes of hexagonal MoS_2. The diffraction spots correspond to the (222), (311), (533) planes of cubic Co_9S_8. This proves the formation of MoS_2 and Co_9S_8 phases in the yolk–shelled polyhedral structures. The energy dispersive spectroscopy (EDS) mapping images (Fig. 2g), showing that Co, C and N are distributed in the core and shell and Mo and S are distributed in the entire yolk–shelled structure, further demonstrate the successful fabrication of the yolk–shelled Co_9S_8/MoS_2–CN structure.

The phases of the samples were further analyzed by XRD. The corresponding patterns are shown in Fig. 3a. In the XRD pattern of the Co_9S_8/MoS_2–CN composite, there are a series of diffraction peaks around 15.5°, 29.9°, 31.2°, 47.4° and 52.0°, which should be indexed to the (111), (311), (222), (511) and (440) planes of cubic Co_9S_8 (JCPDS no. 19-0364). And other peaks at 14.4°, 33.5°, 39.5° and 58.3° can also be observed, which match well with the (002), (101), (103) and (110) planes of hexagonal MoS_2 (JCPDS no. 37-1492). The Raman spectra of the yolk–shelled polyhedral Co_9S_8/MoS_2–CN nanocomposite, Co_9S_8–CN and MoS_2 are shown in Fig. 3b. In the Raman spectra of the Co_9S_8/MoS_2–CN nanocomposite and Co_9S_8–CN, two strong peaks located at 1345 and 1580 cm^{-1} are observed, corresponding to the D-band and G-band of carbon materials. The graphitic degree of carbons can be evaluated from the width of the I_G peak and the ratio of I_D/I_G.[43] The corresponding I_D/I_G ratio (about 1.04) and narrow G band indicate the formation of mainly graphitized carbon, which is thought to be transformed from 2-methylimidazole ligands during the carbonization and sulfuration processes. In addition, compared with the characteristic peak of 470 cm^{-1} for Co_9S_8, and vibration modes of E^1_{2g} at 376 cm^{-1} and A_{1g} at 403 cm^{-1} for MoS_2, slight deviations occur in the spectrum of the Co_9S_8/MoS_2–CN composite. This may be caused by the Co–Mo bond formation at the junction of Co_9S_8 and MoS_2 in the yolk–shelled structures.[44,45] The XRD and Raman results further proved the formation of Co_9S_8/MoS_2–CN composite structures. The N_2 adsorption–desorption isothermal curve of the Co_9S_8/MoS_2–CN composite at 77 K is shown in Fig. S4,† giving a Brunauer–Emmett–Teller (BET) surface area of 13.78 $m^2\ g^{-1}$, which should provide enough

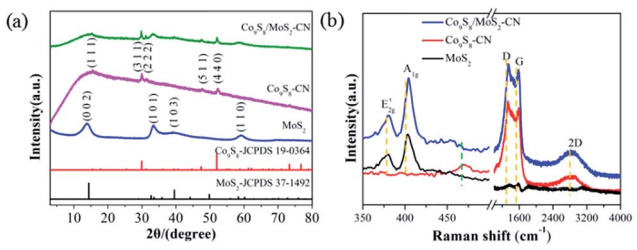

Fig. 3 (a) XRD patterns and (b) Raman spectra of the Co_9S_8/MoS_2–CN composite, Co_9S_8–CN and MoS_2.

active sites for the electrolyte contact when used as an electrode material for SIBs.

The elements and oxidation states of the sample investigated by the X-ray photoelectron spectroscopy (XPS) analysis further verify the five elements of Co, Mo, S, C and N in the composite as shown in Fig. 4. No other elements can be detected as shown in the survey spectrum (Fig. 4a). Fig. 4b displays the high-resolution Co 2p core level XPS spectrum, which can be fitted into six peaks. Two obvious peaks at 793.6 and 778.7 eV separately correspond to Co $2p^{1/2}$ and Co $2p^{3/2}$ for Co^{3+}; two peaks at 798.1 and 782.0 eV originate from Co^{2+} $2p^{1/2}$ and Co^{2+} $2p^{3/2}$, respectively; while two satellite peaks at 802.9 and 785.7 eV can be attributed to the typical peaks for Co^{3+}.[46] In the Mo 3d & S 2s spectrum (Fig. 4d), there are four peaks at 229.5, 232.7, 226.8 and 236.0 eV, which are assigned to Mo^{4+} $3d^{5/2}$, Mo^{4+} $3d^{3/2}$, S 2s and Mo^{6+}, respectively.[45] The appearance of Mo^{6+} (236.0 eV) in the sample is due to the partial oxidization of MoS_2 during exposure to air before XPS measurement.[45] The spectrum in Fig. 4d has two distinct peaks at 162.0 for S $2p^{3/2}$ and 163.2 eV for S $2p^{1/2}$, indicating that sulphur exists as S^{2-} ions. In addition, one more peak at ~169 eV is a shakeup satellite peak.[47,48] Fig. 4e depicts the C 1s spectrum fitted into two peaks at 284.8 and 285.8 eV, which correspond to C–C (sp^2) and C–N, respectively. As for the N 1s core level XPS spectrum (Fig. 4f), three fitted peaks around 398.4, 400.7, and 401.7 eV may be assigned to pyridinic, pyrrolic and graphitic N species.[49] What's more, the mass contents of carbon, Co_9S_8, and MoS_2 in the composite can be roughly calculated to be 27.6%, 17.8%, and 54.6%, respectively, based on the ICP (Table S1†) and the TGA results (Fig. S5†).

To investigate the electrochemical performance of the Co_9S_8/MoS_2–CN composite as an anode material for SIBs, half cells were assembled in an Ar-glovebox. Fig. 6a shows the initial five CV profiles of the Co_9S_8/MoS_2–CN composite electrode in the voltage range of 3.0 to 0.0 V at a scan rate of 0.1 mV s^{-1}. Three peaks can be observed in the first cathodic curve (Fig. 5a). Comparing the CV results of the Co_9S_8/MoS_2–CN composite with those of Co_9S_8–CN and MoS_2 anodes (Fig. S6†), the corresponding electrochemical process may be distinguished for each peak. The broad waves between 0.6 and 0.3 V can be attributed to the formation of solid electrolyte interface (SEI) layers, which lead to irreversible capacity loss and low coulombic efficiency (CE) in the first cycle. The peak between 1.2 and 0.6 V corresponds to the intercalation of Na^+ ions into MoS_2 interlayers to form Na_xMoS_2 and the multi-step reduction of Co_9S_8 into metallic Co and Na_2S. This peak is also observed in the first cathodic curve for the Co_9S_8–CN anode as shown in Fig. S6a,† representing the electrochemical conversion reaction of Co_9S_8 with Na. The sharp peak around 0.11 V originates from the conversion of Na_xMoS_2 into metallic Mo and Na_xS.[50,51] The following four cyclic cathodic curves show nearly the same profiles with two peaks and a tail band. The peaks attributed to the multi-step reduction of Co_9S_8 and the intercalation of Na^+ ions into MoS_2 interlayers move to higher voltages of 1.5 V and 0.85 V, indicating an active process in the first cycle. The tail band around 0 V is considered as the reduction of Na_xMoS_2 into metallic Mo. Accordingly, in the charge process, one main oxidation peak at 1.8 V is observed for the anodic curves, which is attributed to the reversible oxidation process.[38,51] The almost overlapped CV curves in the following four cycles suggest a good reversibility between Na^+ insertion and extraction.

Fig. 5b shows the selected charge–discharge profiles for the 1st, 2nd, 10th, 50th and 100th cycles at 0.5 A g^{-1} in the voltage range of 0.01–3.0 V for the Co_9S_8/MoS_2–CN composite electrode. The slopes are well consistent with the CV results. The first discharge and charge capacities are 840 and 604 mA h g^{-1}, respectively, giving a high first CE of 71.9%. The irreversible capacity loss is mainly due to the formation of a SEI layer during

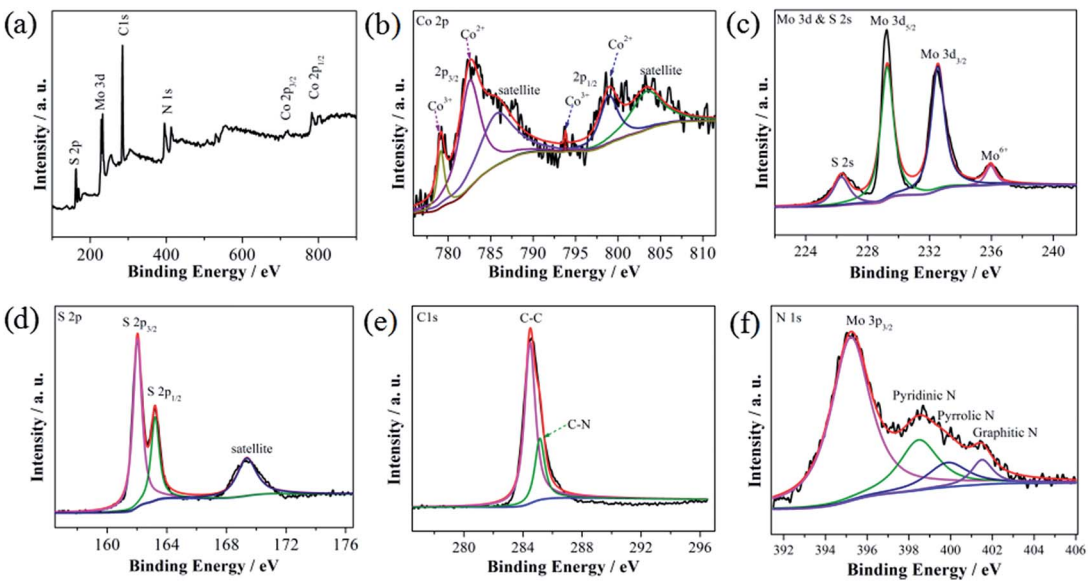

Fig. 4 XPS spectra of the Co_9S_8/MoS_2–CN composite: (a) survey spectrum, (b) Co 2p, (c) Mo 3d & S 2s, (d) S 2p, (e) C 1s, and (f) N 1s core level spectra.

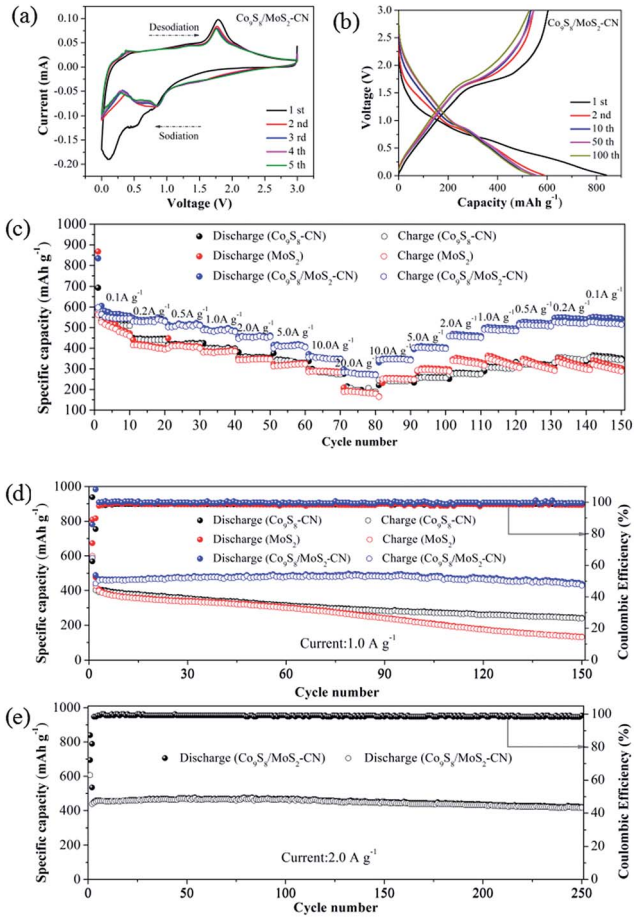

Fig. 5 (a) CV curves at a scan rate of 0.1 mV S^{-1} and (b) charge–discharge profiles at 0.5 A g^{-1} for the Co_9S_8/MoS_2–CN composite; (c) rate capability at different current densities and (d) cycling performance at 1.0 A g^{-1} for the Co_9S_8/MoS_2–CN composite, Co_9S_8–CN and MoS_2 anodes; (e) cycling performance at a high current density of 2.0 A g^{-1} for the Co_9S_8/MoS_2–CN composite. For the cycling performance, the electrodes were cycled at a current density of 0.05 A g^{-1} in the first cycle.

the initial sodiation process.[33] Starting from the 2nd cycle, the discharge/charge profiles are almost identical within 100 cycles. The reversible discharge capacities for the 2nd, 10th, 50th and 100th cycles are respectively 588, 541, 557, and 541 mA h g^{-1} with CEs up to about 98%, revealing the outstanding cycling stability of the Co_9S_8/MoS_2–CN composite anode in SIBs.

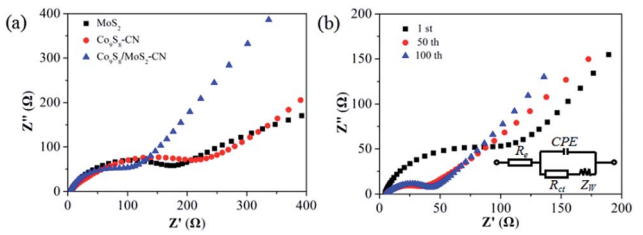

Fig. 6 Nyquist plots of (a) the Co_9S_8/MoS_2–CN composite and Co_9S_8–CN electrodes after 1 cycle, and (b) the Co_9S_8/MoS_2–CN composite electrode after different cycles.

To investigate the superiority of the rate capability and cycling performance of the Co_9S_8/MoS_2–CN composite anode, the electrochemical performances of Co_9S_8–CN and MoS_2 anodes were also measured and are compared as shown in Fig. 5c and d. The rate capability was evaluated at current densities of 0.1, 0.2, 0.5, 1.0, 2.0, 5.0, 10.0 and 20.0 A g^{-1}. And each current density was cycled 10 times. The Co_9S_8/MoS_2–CN composite anode can give a high capacity of 275 mA h g^{-1} even at 20.0 A g^{-1} with a capacity retention of 48.7% in comparison with the capacity at 0.1 A g^{-1}. Under the same conditions, the capacity retention value is only 37.8% and 36.9% for the Co_9S_8–CN and MoS_2 anodes, respectively. Importantly, the discharge capacity of the Co_9S_8/MoS_2–CN composite electrode can be fully recovered to 546 mA h g^{-1} from 275 mA h g^{-1} when the cycling current density is changed from 20.0 A g^{-1} to 0.1 A g^{-1}. However, the discharge capacity of the Co_9S_8–CN electrode only delivers decreased capacities when the cycling current density returns to a low value of 0.1 A g^{-1}. And the cycling performance of the Co_9S_8/MoS_2–CN composite, Co_9S_8–CN and MoS_2 anodes was measured and compared at a current density of 1.0 A g^{-1} as shown in Fig. 5d. For the Co_9S_8/MoS_2–CN composite electrode, the first cycle yields discharge and charge capacities of 834 and 604 mA h g^{-1} at a low current density of 0.05 A g^{-1} with an initial CE of ~72.4%. When the cycling current density increases to 1.0 A g^{-1}, the discharge capacities are stabilized at 438 mA h g^{-1} during the following 150 cycles with CE as high as 98%. This demonstrates the excellent cycling stability of the Co_9S_8/MoS_2–CN composite electrode. As for the Co_9S_8–CN and MoS_2 electrodes, the capacity retention is only 50.0% and 28.1% after 150 cycles under the same cycling conditions, respectively. These results both verify that the Co_9S_8/MoS_2–CN composite possesses better rate and cycling performances than Co_9S_8–CN and MoS_2 electrodes. More importantly, the Co_9S_8/MoS_2–CN composite electrode also shows excellent cycling stability at a high current density of 2.0 A g^{-1} (Fig. 5e). After 250 cycles, it delivers a high specific capacity of 421 mA h g^{-1} with a high capacity retention of 93.2% in comparison with the value in the 3rd cycle. The superior rate and cycling performances of the Co_9S_8/MoS_2–CN composite electrode suggest that after the MoS_2 coating, the ohmic resistance and activation energy for Na^+ ion diffusion are decreased, leading to a fast faradaic reaction, because of short paths enabling fast ion diffusion and a large exposed surface, as well as abundant ion insertion channels providing by the MoS_2 layers.[4,52] And this will support the enhanced high rate cycling performance. In addition, the structures of the Co_9S_8/MoS_2–CN composite after discharge/charge cycling were determined by TEM (Fig. S7†), showing that the yolk–shelled structures can be maintained. This indicates that the yolk–shelled structures are stable and can endure the volume changes during the sodiation/desodiation process, providing the impressive cycling performance.

To understand the outstanding rate and cycling performance of the Co_9S_8/MoS_2–CN composite, electrochemical impedance spectroscopy (EIS) was further performed as shown in Fig. 6. All Nyquist plots are composed of semicircles and straight lines. The semicircle is related to charge transfer resistance (R_{ct}).[1,53,54] After the 1st cycle, the R_{ct} of the Co_9S_8/MoS_2–CN composite is

estimated to be ~55 Ω, which is smaller than those of Co_9S_8–CN and MoS_2 electrodes as shown in Fig. 6a, indicating a superior rate capability of the composite electrode. The R_{ct} values of the Co_9S_8/MoS_2–CN composite electrode gradually reduce upon the increase of cycling times until stabilizing at ~37 Ω after the 100th cycle, indicating superior cycling stability.

The yolk–shelled Co_9S_8/MoS_2–CN nanocomposite exhibits impressive electrochemical performance when used as an anode material for SIBs. This mainly benefits from the unique yolk–shelled structure and the synergistic effect of the *in situ* carbon, Co_9S_8 and MoS_2 in the composite. The yolk–shelled structure can lower diffusion energy barriers and facilitate fast Na^+ ion insertion/extraction reaction kinetics. And the void in the core provides enough space to endure volume changes upon the sodiation/desodiation process. For the synergistic effect, on one hand, the *in situ* formed CN can increase the electrochemical conductivity and increase the active sites for electron transfer between the electrode and the electrolyte. On the other hand, both the Co_9S_8 and MoS_2 in the composite can exploit their own advantages and mutually enhance the electrochemical performance of the Co_9S_8/MoS_2–CN nanocomposite.

Conclusions

In summary, a yolk–shelled Co_9S_8/MoS_2–CN nanocomposite was successfully fabricated using ZIF-67 as the precursor through a step by step processes. Yolk shelled structures were formed based on the heterogeneous contraction caused during the heat treatment process. As an anode material for SIBs, the Co_9S_8/MoS_2–CN nanocomposite exhibits impressive rate capability and cycling performance attributed to its yolk–shelled structures, *in situ* CN coating and synergistic effect. When the test current density increases from 0.1 A g^{-1} to 20.0 A g^{-1}, the Co_9S_8/MoS_2–CN nanocomposite electrode gives a satisfactory capacity of 275 mA h g^{-1} with a capacity retention of 48.7%, which is much higher than 37.8% and 36.9% of Co_9S_8–CN and MoS_2 electrodes, respectively. When cycled at 1.0 A g^{-1}, the discharge capacities are stabilized at 438 mA h g^{-1}, and Co_9S_8–CN and MoS_2 electrodes can only exhibit a capacity retention of 50.0% and 28.1% within 150 cycles, respectively. The excellent electrochemical performance of the Co_9S_8/MoS_2–CN nanocomposite indicates that MOF derived composite materials should attract our attention in the field of energy storage systems such as LIBs and SIBs.

Conflicts of interest

There are no conflicts to declare.

Acknowledgements

This work was financially supported by the National Natural Science Foundation of China (NSFC Grant 51702366, 21371179, and 21771193), Taishan Scholar Foundation (ts201511019), Natural Science Foundation of Shandong Province (ZR2017BB046) and Fundamental Research Funds for the Central Universities (17CX02037A).

Notes and references

1 Z.-T. Shi, W. Kang, J. Xu, L.-L. Sun, C. Wu, L. Wang, Y.-Q. Yu, D. Y. W. Yu, W. Zhang and C.-S. Lee, *Small*, 2015, **11**, 5667–5674.
2 Y. Jiang, M. Wei, J. Feng, Y. Ma and S. Xiong, *Energy Environ. Sci.*, 2016, **9**, 1430–1438.
3 H. Kang, Y. Liu, K. Cao, Y. Zhao, L. Jiao, Y. Wang and H. Yuan, *J. Mater. Chem. A*, 2015, **3**, 17899–17913.
4 W. Kang, Y. Wang and J. Xu, *J. Mater. Chem. A*, 2017, **5**, 7667–7690.
5 F. Niu, J. Yang, N. Wang, D. Zhang, W. Fan, J. Yang and Y. Qian, *Adv. Funct. Mater.*, 2017, **27**, 1700522.
6 W. Zhao, C. Guo and C. M. Li, *J. Mater. Chem. A*, 2017, **5**, 19195–19202.
7 J. Choi, N. R. Kim, K. Lim, K. Ku, H. J. Yoon, J. G. Kang, K. Kang, P. V. Braun, H.-J. Jin and Y. S. Yun, *Small*, 2017, **13**, 1700767.
8 C. Zhao, C. Yu, M. Zhang, Q. Sun, S. Li, M. N. Banis, X. Han, Q. Dong, J. Yang, G. Wang, X. Sun and J. Qiu, *Nano Energy*, 2017, **41**, 66–74.
9 R. S. Babu and M. Pyo, *J. Electrochem. Soc.*, 2014, **161**, A1045–A1050.
10 K.-l. Hong, L. Qie, R. Zeng, Z.-q. Yi, W. Zhang, D. Wang, W. Yin, C. Wu, Q.-j. Fan, W.-x. Zhang and Y.-h. Huang, *J. Mater. Chem. A*, 2014, **2**, 12733–12738.
11 Y. Cao, L. Xiao, M. L. Sushko, W. Wang, B. Schwenzer, J. Xiao, Z. Nie, L. V. Saraf, Z. Yang and J. Liu, *Nano Lett.*, 2012, **12**, 3783–3787.
12 L. Wang, K. Zhang, Z. Hu, W. Duan, F. Cheng and J. Chen, *Nano Res.*, 2014, **7**, 199–208.
13 C. Chu, J. Yang, Q. Zhang, N. Wang, F. Niu, X. Xu, J. Yang, W. Fan and Y. Qian, *ACS Appl. Mater. Interfaces*, 2017, **9**, 43648–43656.
14 Y. Wang, C. Wang, Y. Wang, H. Liu and Z. Huang, *J. Mater. Chem. A*, 2016, **4**, 5428–5435.
15 Y. Zhou, J. Tai, H. Xu, J. Yang and Y. Qian, *Energy Storage Materials*, 2017, **6**, 149–156.
16 J. Li, D. Yan, T. Lu, W. Qin, Y. Yao and L. Pan, *ACS Appl. Mater. Interfaces*, 2017, **9**, 2309–2316.
17 K. Zhang, M. Park, L. Zhou, G.-H. Lee, J. Shin, Z. Hu, S.-L. Chou, J. Chen and Y.-M. Kang, *Angew. Chem., Int. Ed.*, 2016, **128**, 13014–13018.
18 P. He, Y. Fang, X.-Y. Yu and X. W. Lou, *Angew. Chem., Int. Ed.*, 2017, **129**, 12370–12373.
19 Y. Xiao, S. H. Lee and Y.-K. Sun, *Adv. Energy Mater.*, 2017, **7**, 1601329.
20 D. Zhang, W. Sun, Y. Zhang, Y. Dou, Y. Jiang and S. X. Dou, *Adv. Funct. Mater.*, 2016, **26**, 7479–7485.
21 X. Zhang, X. J. Liu, G. Wang and H. Wang, *J. Colloid Interface Sci.*, 2017, **505**, 23–31.
22 Z. Shadike, M.-H. Cao, F. Ding, L. Sang and Z.-W. Fu, *Chem. Commun.*, 2015, **51**, 10486–10489.
23 X. Zhu, X. Jiang, X. Liu, L. Xiao, X. Ai, H. Yang and Y. Cao, *Ceram. Int.*, 2017, **43**, 9630–9635.
24 J. Li, Y. Fu, X. Shi, Z. Xu and Z. Zhang, *Chem.–Eur. J.*, 2017, **23**, 157–166.

25 W. Xia, A. Mahmood, R. Zou and Q. Xu, *Energy Environ. Sci.*, 2015, **8**, 1837–1866.
26 S.-L. Li and Q. Xu, *Energy Environ. Sci.*, 2013, **6**, 1656–1683.
27 L. Wang, Y. Han, X. Feng, J. Zhou, P. Qi and B. Wang, *Coord. Chem. Rev.*, 2016, **307**, 361–381.
28 Q.-L. Zhu, W. Xia, T. Akita, R. Zou and Q. Xu, *Adv. Mater.*, 2016, **28**, 6391–6398.
29 X.-Y. Yu, Y. Feng, Y. Jeon, B. Guan, X. W. Lou and U. Paik, *Adv. Mater.*, 2016, **28**, 9006–9011.
30 R. Wang, D. Jin, Y. Zhang, S. Wang, J. Lang, X. Yan and L. Zhang, *J. Mater. Chem. A*, 2017, **5**, 292–302.
31 S. Zhang, D. Li, S. Chen, X. Yang, X. Zhao, Q. Zhao, S. Komarneni and D. Yang, *J. Mater. Chem. A*, 2017, **5**, 12453–12461.
32 L. Zhou, K. Zhang, J. Sheng, Q. An, Z. Tao, Y.-M. Kang, J. Chen and L. Mai, *Nano Energy*, 2017, **35**, 281–289.
33 H. Li, Y. Su, W. Sun and Y. Wang, *Adv. Funct. Mater.*, 2016, **26**, 8345–8353.
34 J. Xiang and T. Song, *Chem. Commun.*, 2017, **53**, 10820–10823.
35 Z. Chen, R. Wu, M. Liu, H. Wang, H. Xu, Y. Guo, Y. Song, F. Fang, X. Yu and D. Sun, *Adv. Funct. Mater.*, 2017, **27**, 1702046.
36 F. Zou, Y.-M. Chen, K. Liu, Z. Yu, W. Liang, S. M. Bhaway, M. Gao and Y. Zhu, *ACS Nano*, 2016, **10**, 377–386.
37 K. J. Zhu, G. Liu, Y. J. Wang, J. Liu, S. T. Li, L. Y. Yang, S. L. Liu, H. Wang and T. Xie, *Mater. Lett.*, 2017, **197**, 180–183.
38 Z. Zhang, Y. Gan, Y. Lai, X. Shi, W. Chen and J. Li, *RSC Adv.*, 2015, **5**, 103410–103413.
39 J. Li, D. Yan, X. Zhang, S. Hou, T. Lu, Y. Yao and L. Pan, *J. Mater. Chem. A*, 2017, **5**, 20428–20438.
40 S. Dong, C. Li, X. Ge, Z. Li, X. Miao and L. Yin, *ACS Nano*, 2017, **11**, 6474–6482.
41 Y. Zhang, A. Pan, L. Ding, Z. Zhou, Y. Wang, S. Niu, S. Liang and G. Cao, *ACS Appl. Mater. Interfaces*, 2017, **9**, 3624–3633.
42 B. Y. Guan, A. Kushima, L. Yu, S. Li, J. Li and X. W. Lou, *Adv. Mater.*, 2017, **29**, 1605902.
43 J. Robertson, *Mater. Sci. Eng., R*, 2002, **37**, 129–281.
44 H. Zhu, J. Zhang, R. Yanzhang, M. Du, Q. Wang, G. Gao, J. Wu, G. Wu, M. Zhang, B. Liu, J. Yao and X. Zhang, *Adv. Mater.*, 2015, **27**, 4752–4759.
45 J. Shao, T. Gao, Q. Qu, Q. Shi, Z. Zuo and H. Zheng, *J. Power Sources*, 2016, **324**, 1–7.
46 Y. Li, J. Liu, C. Chen, X. Zhang and J. Chen, *ACS Appl. Mater. Interfaces*, 2017, **9**, 5982–5991.
47 J. Wang, J. Liu, D. Chao, J. Yan, J. Lin and Z. X. Shen, *Adv. Mater.*, 2014, **26**, 7162–7169.
48 H. Geng, J. Yang, Z. Dai, Y. Zhang, Y. Zheng, H. Yu, H. Wang, Z. Luo, Y. Guo, Y. Zhang, H. Fan, X. Wu, J. Zheng, Y. Yang, Q. Yan and H. Gu, *Small*, 2017, **13**, 1603490.
49 H. Dong, C. Liu, H. Ye, L. Hu, B. Fugetsu, W. Dai, Y. Cao, X. Qi, H. Lu and X. Zhang, *Sci. Rep.*, 2015, **5**, 17542.
50 X. Xiong, W. Luo, X. Hu, C. Chen, L. Qie, D. Hou and Y. Huang, *Sci. Rep.*, 2015, **5**, 9254.
51 Z.-T. Shi, W. Kang, J. Xu, Y.-W. Sun, M. Jiang, T.-W. Ng, H.-T. Xue, D. Y. W. Yu, W. Zhang and C.-S. Lee, *Nano Energy*, 2016, **22**, 27–37.
52 J.-Y. Liao, B. D. Luna and A. Manthiram, *J. Mater. Chem. A*, 2016, **4**, 801–806.
53 Z. Li, L. Zhang, X. Ge, C. Li, S. Dong, C. Wang and L. Yin, *Nano Energy*, 2017, **32**, 494–502.
54 Q. Tang, Y. Cui, J. Wu, D. Qu, A. P. Baker, Y. Ma, X. Song and Y. Liu, *Nano Energy*, 2017, **41**, 377–386.

